Delft University of Technology

Marchenko imaging by unidimensional deconvolution

M. A. Matias, Mayara; da C. Pestana, Reynam; van der Neut, Joost

DOI
10.1111/1365-2478.12686

Publication date
2018

Document Version
Accepted author manuscript

Published in
Geophysical Prospecting

Citation (APA)
M. A. Matias, M., da C. Pestana, R., & van der Neut, J. (2018). Marchenko imaging by unidimensional deconvolution. *Geophysical Prospecting*. https://doi.org/10.1111/1365-2478.12686

Important note
To cite this publication, please use the final published version (if applicable).
Please check the document version above.

Copyright
Other than for strictly personal use, it is not permitted to download, forward or distribute the text or part of it, without the consent of the author(s) and/or copyright holder(s), unless the work is under an open content license such as Creative Commons.

Takedown policy
Please contact us and provide details if you believe this document breaches copyrights.
We will remove access to the work immediately and investigate your claim.

This work is downloaded from Delft University of Technology.
For technical reasons the number of authors shown on this cover page is limited to a maximum of 10.

Marchenko imaging by unidimensional deconvolution

Mayara M. A. Matias[1], Reynam da C. Pestana[2], Joost van der Neut[3][4]

[1]Federal University of Bahia (UFBA) and Petróleo Brasileiro S.A. (PETROBRAS). Rua Barão de Geremoabo, Salvador, Bahia, Brazil. E-mail: maya.matiass@gmail.com

[2]Federal University of Bahia (UFBA), Center for Research in Geophysics and Geology (CPGG) and National Institute of Science and Technology of Petroleum Geophysics (INCT-GP/CNPQ). Rua Barão de Geremoabo, Salvador, Bahia, Brazil. E-mail: pestana.reynam@gmail.com

[3]Delft University of Technology (TU Delft), Department of Imaging Physics. Lorentzweg 1, 2628 CJ Delft, The Netherlands. E-mail: J.R.vanderNeut@tudelft.nl

[4]The authors have no conflict of interest to declare.

Seismic; Imaging

Abstract

Obtaining an accurate image of the subsurface still remains a great challenge for the seismic method. Migration algorithms aim mainly on positioning seismic events in complex geological contexts. Multiple reflections are typically not accounted for in this process, which can lead to the emergence of artifacts. In Marchenko imaging, we retrieve the complete up- and downgoing wavefields in the subsurface to construct an image without such artifacts. The quality of this image depends on the type of imaging condition that is applied. In this paper, we propose an imaging condition that is based on stabilized unidimensional deconvolution. This condition is computationally much cheaper than multidimensional deconvolution, which has been proposed for Marchenko imaging earlier. Two specific approaches are considered. In the first approach, we use the full up- and downgoing wavefields for deconvolution. Although this leads to balanced and relatively accurate amplitudes, the crosstalk is not completely removed. The second approach is to incorporate the initial focusing function in the deconvolution process, in such a way that the retrieval of crosstalk is avoided. We compare images with the results of the classical cross-correlation imaging condition, which we apply to reverse-time migrated wavefields and to the up- and downgoing wavefields that are retrieved by the Marchenko method.

1 Introduction

Seismic imaging methods are heading for better resolution images, in a sense that more information can be extract from them. Interpreters should be able to recognize the limitations of the dataset they are working with and be presented to a range of possible solutions for obtaining material parameters as accurate as possible to achieve less uncertainty in decision making.

Prestack reverse-time migration (RTM) presents itself as the most robust imaging tool commercially in use. It is based on the two-way wave equation solution, simulating wavefield propagation in all directions accurately, including reflections and transmissions, with no restriction of steeply dipping structures, which allows for imaging through complex media. But even such sophisticated method has some drawbacks for it relies on the single-scattering assumption, which means that the imaging process does not take in account multiply-scattered events, assuming all reflections are primary (Figure 1). This has two major implications: multiple reflections should be eliminated prior to the migration process; and ghost reflectors will appear on the final image in case this elimination is not efficient, which can lead to misinterpretation.

Nowadays there is an important discussion on whether to incorporate the information given by multiples in the imaging process for it may improve illumination (Berkhout, 2017). Marchenko imaging (Thorbecke et al., 2013; Behura et al., 2014; Broggini et al., 2014b,a; Wapenaar et al., 2014b; Meles et al., 2016; da Costa Filho et al., 2017; Singh et al., 2017) shows up as a novel target-oriented method that takes multiples into account and provides cleaner images with more reliable amplitudes. Although some limiting assumptions have to be made (*e.g.*, lossless media, infinite aperture, among others), provided the same inputs as conventional migration algorithms (*i.e.*, pre-conditioned observed data and a velocity model with the best possible resolution) the technique is showing promising results on the proposed subject as shown in mentioned works above. Several other methods are being developed that utilize multiply-scattered events during the migration process (Wang et al., 1999; Zhou et al., 2003; Guitton, 2002; Muijs et al., 2007; Malcolm et al., 2009; Ong et al., 2013; Fleury, 2013; Berkhout and Verschuur, 2006; Weglein et al., 2003), but the comparison between these and Marchenko's solution is not part of the scope in this paper.

When it comes to utilizing multiple reflections, it is critical to account for free-surface multiples as well as internal multiple reflections. Berkhout (2017) addresses this issue as a "plea made to say farewell to investments in multiple *removal* algorithms". Adapting the Marchenko method to account for the combined surface-related and internal multiples effects is an ongoing research effort. Only very recently free-surface effects have been incorporated in Marchenko equation. Singh and Snieder (2017) have adjusted the methodology to accommodate free-surface multiples as well. However, it has been shown that solving for the Marchenko's equation based on the previously established iterative scheme may not always converge, and hence new approaches have been proposed such as we may see in the works of Dukalski and de Vos (2017) and Staring et al. (2017). Alternative inversion schemes have been proposed if one assumes that the wavefield is recorded such that the vertical particle velocity data is properly sampled and can be obtained in separate up- and downgoing components (Slob and Wapenaar, 2017; Ravasi, 2017).

In this work, we apply Marchenko imaging. This imaging method is composed of wavefield extrapolation and image condition steps, as any other kind of migration technique. The first step in this case is specifically known as Marchenko *redatuming* that consists of an iterative autofocusing scheme that allows for retrieving the up- and downgoing Green's functions at any desired focal point in the subsurface one intends to image. These components of the Green's function are the imaging operators we work on in this paper, assessing the results of applying different image conditions that reckon multiply-scattered reflections. Our main goal is to apply Marchenko imaging with a deconvolution-based imaging condition, relying on a stabilized unidimensional deconvolution approach. This is different from the multidimensional deconvolution imaging condition (MDD) of Broggini et al. (2014b), and our proposed imaging condition is computationally much cheaper. We compare the results with the RTM image that makes use of the classic correlation-based imaging condition.

Hence, we start by briefly presenting Marchenko redatuming exerting the iterative so-called conventional scheme (Thorbecke et al., 2017). After that, we describe the proposed imaging conditions and depict the obtained results for two synthetic models. One last observation we need to point out is that we deal with the acoustic case and do not incorporate free surface-related multiples, since this is still under very recent investigation and we make use of the iterative scheme. Therefore, we consider a transparent acquisition surface, given that our numerical examples involve synthetic models. For real data, in practice, all surface-related multiples should be removed from the reflection response (Verschuur et al., 1992; Amundsen, 2001) prior to Green's functions retrieval to accommodate for this limitation, which is no different from industry's *modus operandi* currently in conventional pre-migration processing workflows.

2 The iterative Marchenko method

From reciprocity theorems of correlation and convolution types between two states (de Hoop, 1995; Wapenaar and Grimberg, 1996; Slob et al., 2014; Wapenaar et al., 2014a; van der Neut et al., 2015) and based on inverse scattering theory (Broggini and Snieder, 2012), it is possible to relate wavefields that focus the energy in a specific focal point in the subsurface to the Green's function relative to this point that is recognized as a virtual source. These wavefields are known as focusing functions or focusing solutions and the relation to the up- and downgoing Green's function component at the selected point in subsurface is given by

$$\int_{S_a} dx\, [\hat{f}_1^+(x, z_0; x', z_i)\hat{R}(x, z_0; x'', z_0)] - \hat{f}_1^-(x'', z_0; x', z_i) = \hat{G}^-(x', z_i; x'', z_0), \tag{1}$$

and

$$\hat{f}_1^+(x'', z_0; x', z_i) - \int_{S_a} dx\, [\hat{f}_1^-(x, z_0; x', z_i)\hat{R}^*(x, z_0; x'', z_0)] = \hat{G}^{+*}(x', z_i; x'', z_0). \tag{2}$$

In equations (1) and (2), the down- and upgoing focusing functions in the frequency domain, $\hat{f}_1^+(x, z_0; x', z_i)$ and $\hat{f}_1^-(x'', z_0; x', z_i)$, respectively, are defined in a modified medium that is homogeneous below z_i. These correspond to solutions to the wave equation that focus at zero-time at the determined subsurface point x', z_i, and then continue as downgoing diverging fields into a lower homogeneous half-space. They are injected from the surface datum S_a (x, z_0). Moreover, $\hat{G}^-(x', z_i; x'', z_0)$ and $\hat{G}^+(x', z_i; x'', z_0)$ are the up- and downgoing Green's function components, respectively, also in frequency domain, with a source at the acquisition surface S_a (x'', z_0), and a receiver at the desired focal point in subsurface x', z_i, which belong to the wave state of the physical world where data $\hat{R}(x, z_0; x'', z_0)$ are acquired. The superscript '*' corresponds to the complex conjugate of the wavefield, which corresponds to time-reversal in time domain.

Equations (1) and (2) comprehend the Green's functions representation and these wavefields are the ones we aim to obtain for the redatuming purpose. If we write these equations in the time domain, we get (Slob et al., 2014; Wapenaar et al., 2014a):

$$f_1^-(x'', z_0; x', z_i; t) + G^-(x', z_i; x'', z_0; t) = \\ = \int_{S_a} \mathrm{d}x \int \mathrm{d}\tau R(x, z_0; x'', z_0; t-\tau) f_1^+(x, z_0; x', z_i; \tau), \quad (3)$$

and

$$f_1^+(x'', z_0; x', z_i; t) - G^+(x', z_i; x'', z_0; -t) = \\ \int_{S_a} \mathrm{d}x \int \mathrm{d}\tau R(x, z_0; x'', z_0; t+\tau) f_1^+(x, z_0; x', z_i; \tau). \quad (4)$$

Pursuing the simplicity of the matrix notation (van der Neut et al., 2015), we achieve:

$$\begin{cases} \mathbf{f}_1^- + \mathbf{g}^- = \mathbf{R}\mathbf{f}_1^+ \\ \mathbf{f}_1^+ - \mathbf{g}^{+*} = \mathbf{R}^*\mathbf{f}_1^-, \end{cases} \quad (5)$$

where now we have $\mathbf{R}$ as a convolutional matrix operator containing the reflection response acquired acting on the focusing functions $\mathbf{f}_1^-$ and $\mathbf{f}_1^+$ (stored as vectors). And $\mathbf{R}^*$ is a correlational matrix for the same purpose.

We suppose that $\mathbf{f}_1^+$ may be decomposed into a first arrival/direct wave $\mathbf{f}_{1d}^+$ and a scattering coda $\mathbf{f}_{1coda}^+$ in such a way that $\mathbf{f}_1^+ = \mathbf{f}_{1d}^+ + \mathbf{f}_{1coda}^+$. It can be shown that $\mathbf{f}_{1d}^+$ is the inverse of the transmission response according to the relation:

$$\mathbf{i} = \mathbf{T}_d \mathbf{f}_{1d}^+, \quad (6)$$

where $\mathbf{i}$ is a vector having only one non-zero element at $t = 0$ and $(x = x')_{z=z_i}$, being the location of the chosen focal point (*i.e.*, imaging point). The term $\mathbf{T}_d$ is defined in a similar way as $\mathbf{R}$. This matrix applies multidimensional convolution with the direct transmission response from the imaging point in the subsurface to the sources at the acquisition surface S_a.

Resorting the causality properties of the focusing solutions and the Green's functions, we can apply a window matrix Θ that imposes a causality condition to the underdetermined system (5) (schematically represented by Figure 2), which is designed such that $\Theta\mathbf{g}^- = 0$, $\Theta\mathbf{g}^{+*} = 0$, $\Theta\mathbf{f}_1^+ = \mathbf{f}_{1coda}^+$ and $\Theta\mathbf{f}_1^- = \mathbf{f}_1^-$, as demonstrated by the referenced authors.

Hence, applying the window matrix to the system (5), it is now possible to solve the coupled Marchenko equations for the focusing functions by solving the system of equations:

$$\begin{cases} \mathbf{f}_1^- = \Theta\mathbf{R}\mathbf{f}_{1d}^+ + \Theta\mathbf{R}\mathbf{f}_{1coda}^+ \\ \mathbf{f}_{1coda}^+ = \Theta\mathbf{R}^*\mathbf{f}_1^-. \end{cases} \quad (7)$$

The pseudocode 1 depicts an iterative method to solve the system above from a known initial focusing function $\mathbf{f}_{1d}^{+}$ and the reflection response $\mathbf{R}$. The initial focusing function, $\mathbf{f}_{1d}^{+}$, can be approximated by the time-reversed first arrival of a Green's function as computed in a background velocity model (Broggini et al., 2014b). For very complex geological situation, better approximations can be obtained by inverting the transmission response (Vasconcelos et al., 2014, 2015).

From this, it is finally possible to retrieve the Green's function components at the subsurface point we desire to image. When the focusing functions are retrieved by solving equation (7), the Green's functions can be computed by extracting from system of equations (5) that

$$\begin{cases} \mathbf{g}^{-} = \Psi\mathbf{R}\mathbf{f}_{1d}^{+} + \Psi\mathbf{R}\mathbf{f}_{1coda}^{+}, \quad \text{and} \\ \mathbf{g}^{+*} = \mathbf{f}_{1d}^{+} - \Psi\mathbf{R}^{*}\mathbf{f}_{1}^{-}, \end{cases} \tag{8}$$

where $\Psi = \mathbf{I} - \Theta$, with $\mathbf{I}$ being the identity matrix.

Pseudocode 1 Iterative Green's functions retrieval

1. Conventional pre-processing of observed data;
2. Direct arrivals computation through conventional velocity model:

   Modeling of $G_d(x'', z_0; x', z_i; -t) \rightarrow \mathbf{T}_d^{inv}$

3. Iterative scheme for the focusing functions:

   $\mathbf{f}_{1d}^{+} = \mathbf{T}_d^{*}\delta$! initial focusing function (from equation (6))
   $\mathbf{f}_{1coda}^{+(0)} = 0.$! coda for initial focusing function

   DO k = 1, niter
   $\mathbf{f}_{1}^{-(\mathrm{k})} = \Theta\mathbf{R}\mathbf{f}_{1d}^{+} + \Theta\mathbf{R}\mathbf{f}_{1coda}^{+(\mathrm{k}-1)}$
   $\mathbf{f}_{1coda}^{+(\mathrm{k})} = \Theta\mathbf{R}^{*}\mathbf{f}_{1}^{-(\mathrm{k})}$
   IF convergence ok THEN ; *STOP*
   ELSE ; k = k + 1
   ENDIF
   END DO

4. Green's components retrieval for new datum:

   $\mathbf{g}^{-} = \Psi\mathbf{R}\mathbf{f}_{1d}^{+} + \Psi\mathbf{R}\mathbf{f}_{1coda}^{+}$
   $\mathbf{g}^{+*} = \mathbf{f}_{1d}^{+} - \Psi\mathbf{R}^{*}\mathbf{f}_{1}^{-}$

3 On the imaging conditions

Applying the imaging condition is the step that consolidates the imaging process of any migration algorithm. In possession of the extrapolated wavefields, these are cross-correlated to build an image following Claerbout's imaging principle, by taking the zero lag of this operation (Claerbout, 1971; Chang and

McMechan, 1986).

Dealing with prestack data and referring to reverse-time migration, to migrate the registered data of one shot, meaning $R(x'', z_0; x, z_0; t)$ for a source at $(x, z = 0)$ and receivers at $(x'', z = 0)$, it is necessary to compute the wavefield that originates from the source and to backpropagate the wavefield that was sensed by the receivers. The source wavefield p_s expands following a solution of the full wave equation for constant density

$$\left[\frac{1}{c^2(\mathbf{x})}\frac{\partial^2}{\partial t^2} - \nabla^2\right] p_s(\mathbf{x}, t) = \delta(x - x'')_{z=z_0} f(t), \tag{9}$$

where the spatial coordinates are given by $\mathbf{x} = (x, z)$, x and z are the horizontal and vertical (depth) coordinates, respectively; $c(\mathbf{x})$ is the velocity of the medium; the right-side term constitutes the source term as designated by the delta function, with a band-limited spectrum defined by $f(t)$; and

$$\nabla^2 p_s \equiv \frac{\partial^2 p_s}{\partial x^2} + \frac{\partial^2 p_s}{\partial z^2}, \tag{10}$$

corresponding to the Laplacian operator applied to $p_s(\mathbf{x}, t)$. The receivers wavefield p_r is propagated backward in time following a solution for

$$\left[\frac{1}{c^2(\mathbf{x})}\frac{\partial^2}{\partial t^2} - \nabla^2\right] p_r(\mathbf{x}, t) = 0, \tag{11}$$

where $p_r(\mathbf{x}, t) = R(x'', z_0; x, z_0; t)$ at the acquisition surface (Zhang et al., 2007).

In practice, the imaging condition is implemented by extrapolating both wavefields separately and cross-correlating them at each time step as schematically depicted in Figure 3 and expressed as

$$I(x, z) = \sum_{\mathrm{n}x_s} \sum_{t=0}^{t_{max}} p_s(x, z, t) p_r(x, z, t), \tag{12}$$

where $\mathrm{n}x_s$ is the number of acquisition shots; $t = 0$ is the initial forward propagation time from the source on the surface; t_{max} is the maximum propagation time, that corresponds to total register time; $p_s(x, z, t)$ represents the modeled source wavefield from initial to maximum time; and finally $p_r(x, z, t)$ represents the receivers backpropagated wavefield from maximum to minimum time ($t = 0$). The reflector image will be built where the wavefields are coincident in time.

Benefiting from the iterative scheme presented at the redatuming section, for the Marchenko imaging the equivalent of the receivers' wavefield is the upgoing Green's function $\hat{G}^-$ in the frequency domain, and the downward field analogous to the source wavefield is the downgoing $\hat{G}^+$. In possession of the retrieved decomposed Green's function, it is possible to apply multidimensional deconvolution – MDD (Wapenaar et al., 2008; van der Neut et al., 2011) – relying on (Wapenaar et al., 2000):

$$G^-(x', z_i; x, z_0, t) = \int_{S_f} \mathrm{d}x' \int_{-\infty}^{+\infty} \mathrm{d}\tau \, R_f(x, z_i; x', z_i, \tau) G^+(x', z_i; x'', z_0, t - \tau). \tag{13}$$

$R_f(x, z_i; x', z_i, \tau)$ would then be the optimal result of Marchenko imaging, as claimed in literature (Wapenaar et al., 2014b; Broggini et al., 2014b; Singh et al., 2017). However, this imaging condition is very expensive. Equation (13) should be inverted and solved for $R_f(x, z_i; x', z_i, \tau)$ at different depth levels $z = z_i$ and many image points.

To save computation time, it is suggested to apply the classic cross-correlation imaging condition using these components of the Green's function (Behura et al., 2014), expressed as

$$I_{cc}(\mathbf{x}_I) = \sum_{\mathbf{x}_S} \sum_{\omega} \hat{G}^{-}(\mathbf{x}_I, \mathbf{x}_S) \hat{G}^{+*}(\mathbf{x}_I, \mathbf{x}_S), \tag{14}$$

where now $(x', z_i) = \mathbf{x}_I$ for the focal point coordinates in the subsurface, and $(x'', z_0) = \mathbf{x}_S$ for the sources/receivers position at the original acquisition surface S_a. Yet, this yields inaccurate amplitudes and crosstalk noise.

Adding complexity to honor the reflection physics and trying to compensate for the amplitude loss inherent to the cross-correlation imaging condition, we implemented an unidimensional deconvolution imaging condition (Claerbout, 1971; Valenciano and Biondi, 2003) with a stabilization factor as derived by Ortiz (2015).

The deconvolution imaging condition as initially proposed by Claerbout (1971) consists of a division of the upgoing wavefield by the downgoing one. It is important given that it provides a better illumination compensation and amplitude recovery of the reflectors. However, application of this condition requires caution, because the denominator might be zero at some points. Consequently, some kind of stabilization becomes necessary to avoid division by zero. A simple way to overcome this problem is to add a stability factor, ϵ, to the downgoing wavefield modulus, $|W_S|$, where the value of the factor might be chosen empirically.

In practice, the result may be very sensitive to the stability factor that substitutes for the small values of $|W_S|$, and an improper value of ϵ could lead to a strong smoothing. Setting the imaging condition to zero for values of $|W_S|$ smaller than ϵ is another form of stabilization, evading from wrong amplitudes caused by the choice of an ϵ value with poor criteria, on the other hand. The work of Schleicher et al. (2008) presents an analysis on this very specific kind of stabilization for deconvolution imaging condition. The authors show how migration artifacts are enhanced, which leads to a ringing of amplitudes along reflectors, although the degree of enhancement varies and the reflector images are better equalized.

In this work, the choice of the stabilization implemented is based on Taylor's expansion, where the division issue becomes a geometric series. Therefore, ϵ's value is defined in an adaptive way as a function of the downgoing wavefield spectrum average value, W_S. In this case, if stable, the division behaves better and the result becomes more reliable when compared to the deconvolution imaging condition as stated by Claerbout (1971). For this reason, using the proposed method, the division by zero is averted and the provided results are more reliable, as it will be seen in the synthetic examples section.

Following the arguments and reasoning above, we now have:

$$I_{sd}(\mathbf{x}_I) =$$

$$
\begin{cases}
\sum_{\mathbf{x}_S}\sum_{\omega} \frac{\hat{G}^-(\mathbf{x}_I,\mathbf{x}_S)\hat{G}^{+*}(\mathbf{x}_I,\mathbf{x}_S)}{\overline{W}_S}, & \text{if } \overline{W}_S > \alpha\phi_0; \\
\sum_{\mathbf{x}_S}\sum_{\omega} \frac{\hat{G}^-(\mathbf{x}_I,\mathbf{x}_S)\hat{G}^{+*}(\mathbf{x}_I,\mathbf{x}_S)}{\overline{W}_S} \left(2-\frac{\overline{W}_S}{\alpha\phi_0}\right)\left[1+\left(1-\frac{\overline{W}_S}{\alpha\phi_0}\right)^2\right], & \text{if } \overline{W}_S \leq \alpha\phi_0,
\end{cases}
\tag{15}
$$

where the subscript '*sd*' refers to stabilized deconvolution image condition. In equation (15), $\overline{W}_S$ represents the autocorrelation of downgoing wavefield averaged over the source positions along the surface, (in other words, spectrum average value of this wavefield referred above) meaning:

$$
\overline{W}_S = \sum_{\mathbf{x}_S} \frac{\hat{G}^+(\mathbf{x}_I,\mathbf{x}_S)\hat{G}^{+*}(\mathbf{x}_I,\mathbf{x}_S)}{N_{\mathbf{x}_S}}, \tag{16}
$$

where $N_{\mathbf{x}_S}$ is the number of shot positions at the surface. Yet, α may take values between 0 and 1 (we use an empiric value of 0.2); and the ϕ_0 term represents the average value of the downgoing wavefield for all frequencies, and as so, it's represented as:

$$
\phi_0 = \frac{1}{n_\omega}\sum_{n_\omega} \overline{W}_S, \tag{17}
$$

where n_ω corresponds the number of frequencies that represent the wavefield in the frequency domain.

The numerator of equation (15) still contains crosstalk noise, because the $\hat{G}^+$ component consists of additional events apart from the first arrival. It is crosstalk between deep events in G^- and multiples in G^+ (also deep events). This noise is not compensated by the denominator's accuracy. While unidimensional deconvolution comprises an amplitude balancing, it leaves such crosstalk in place.

Since these artifacts are caused by interaction of multiples in G^+ and primaries (plus multiples) in G^-, they can be avoided by removing the multiples in G^+, but not by removing the multiples in G^-. Therefore, we address removing them from G^+ substituting $\hat{G}^{+*}$ by the initial focusing function, $\hat{f}^+_{1d}$, in a sense that we now can have the following imaging condition:

$$
I_{df}(\mathbf{x}_I) =
$$

$$
\begin{cases}
\sum_{\mathbf{x}_S}\sum_{\omega} \frac{\hat{G}^-(\mathbf{x}_I,\mathbf{x}_S)\hat{f}^+_{1d}(\mathbf{x}_I,\mathbf{x}_S)}{\overline{W}_S}, & \text{if } \overline{W}_S > \alpha\phi_0; \\
\sum_{\mathbf{x}_S}\sum_{\omega} \frac{\hat{G}^-(\mathbf{x}_I,\mathbf{x}_S)\hat{f}^+_{1d}(\mathbf{x}_I,\mathbf{x}_S)}{\overline{W}_S} \left(2-\frac{\overline{W}_S}{\alpha\phi_0}\right)\left[1+\left(1-\frac{\overline{W}_S}{\alpha\phi_0}\right)^2\right], & \text{if } \overline{W}_S \leq \alpha\phi_0,
\end{cases}
\tag{18}
$$

where subscript '*df*' refers to the stabilized deconvolution imaging condition using the initial focusing function. And now we have

$$
\overline{W}_S = \sum_{N_{\mathbf{x}_S}} \frac{\hat{G}^+(\mathbf{x}_I,\mathbf{x}_S)\hat{f}^+_{1d}(\mathbf{x}_I,\mathbf{x}_S)}{N_{\mathbf{x}_S}}. \tag{19}
$$

Hence, this stabilized imaging condition that incorporates the initial focusing function allows for removal of ghost artifacts and balancing of the amplitudes at a much lower cost as MDD would require.

In regard to an extension to 3D, the distinction between the approached processes should be clear from the whole work presented above: one is the Marchenko redatuming process; and the other, the imaging condition we propose to apply. Applying the Marchenko redatuming in 3D is feasible, though expensive, as demonstrated by the recently presented work of Lomas and Curtis (2018). The implementation of the cross-correlation imaging condition is easy and relatively cheap. The method needs the Green's function components, as well as the focusing functions, to be stored in disk, or to be computed during the process, as was done for the 2D case. For the deconvolution-based imaging conditions, we need only to obtain the maximum to proceed the normalization. Then, the expansion should be performed. Therefore, for the imaging condition, the cost is very little, for either of the cases, if we compare to the time expended on the Green's function retrieving by the Marchenko method itself.

Finally, we may summarize the Marchenko process schematically for a single image point (see Figure 4).

4 Results from synthetic data

We now present the results for two synthetic datasets by applying the three discussed imaging conditions for Marchenko's imaging operators: cross-correlation, stabilized unidimensional deconvolution, and stabilized unidimensional deconvolution resorting the initial focusing function. We depict these results by comparing them with the image obtained via RTM applying the classic (correlation-based) imaging condition on the extrapolated two-way wavefields.

The models are chosen for specific purposes. The model[1] is a well-known example for related work on the Marchenko solution (Wapenaar et al., 2014b; Singh et al., 2017) and illustrates the interbed reflections issue remarkably well, so this may be considered a benchmark. The other selected model is intended to represent a more realistic geological situation, given that it is based on a real data model.

For both models, wavefields are generated by a finite differences algorithm by Thorbecke and Draganov (2011) (this algorithm considers second and forth order approximations in time and space, respectively) using velocity and density models. The traveltimes of the direct arrivals were computed from the eikonal equation solver as proposed by Faria and Stoffa (1994). These traveltimes were convolved with a Ricker wavelet to construct our estimated direct arrival. We should emphasize that the acquisition surface is made transparent to avoid the presence of free surface-related multiples.

All RTM final responses are computed by combining the rapid expansion method (*i.e.*, REM) and pseudospectral modeling solutions of the complete wave equation for forward and backward propagation of the wavefields (Pestana and Stoffa, 2010). Moreover, the obtained images were filtered making use of a Laplacian filter (Santos et al., 2012) to attenuate the peculiar low frequency noise inherent to the cross-correlation of the full-wavefields used in the RTM method.

4.1 Syncline model

The velocity and density models for the syncline model are shown in Figure 5. The sample interval used for modeling was 10 m for receivers as well as for sources. We observe the synform feature filled up with

[1]Extracted from the demo open source code provided by Jan Thorbecke, referenced as a work of Thorbecke and Draganov (2011).

horizontal layers at the upper half of the model, a small velocity inversion in relation to the layer right above the interface around 1200 m, and a subtle ramp at the lower half of the model. Density values in the upper part of the model expose very strong contrasts, so that interbed reflections are significant.

Four redatumed fields were selected from two depth levels to illustrate how the reflectors are formed based on Claerbout imaging principle. Figure 6(a) explains the image construction schematically as a cross-correlation or deconvolution process of the up- and downgoing Green's function for depth 1100 m which are shown in Figures 6(b) and 6(c). Figure 7(a) depicts the case where no reflector is imaged given that events for such depth (1000 m in this case) (Figures 7b and 7c) are not coincident in time.

When observing the conventional imaging result (Figure 8a – RTM/cross-correlation imaging condition on full wavefields), the imaged ghost reflectors are easily noticeable. The results of the Marchenko imaging for the same delimited area shown for the RTM image (-2000 m $\leq x' \leq 2000$ m and 100 m $\leq z_i \leq 1700$ m, a total of 64561 points imaged) are depicted in Figure 8(b – d). The efficiency of the method in attenuating the harmful ghost reflections is very clear for any imaging condition resorted.

Nonetheless, besides inaccurate amplitudes, we may still observe a weak copy of the syncline structure between 300 m and 500 m in Figure 8(b). In Figure 8(c), this artifact is not completely removed, since unidimensional deconvolution acts only as an amplitude balancing process. Assessing the result obtained in Figure 8(d), we now verify that the ghost artifacts are completely removed, and amplitudes are well balanced.

So we may conclude that we achieve an image free from crosstalk noise and ghost reflectors/artifacts, with more reliable amplitudes, at a much lower cost compared to MDD, only by applying the stabilized imaging condition which makes use of the initial focusing function.

4.2 Santos Basin model

For this example (Figure 9), the density values for the synthesized model were obtained regarding Gardner's velocity-density relation (Gardner et al., 1974). The selected focal points cover an area of 201 by 201 points (-2000 m $\leq x' \leq 2000$ m and 100 m $\leq z_i \leq 1700$ m, a total of 40401 points imaged) in a grid where horizontal sampling is 10 m between receivers and between sources as well. The imaged area coincides with the shallow portion of the thin layered structure. This area represents a part of a sedimentary basin for marine environment systems, as we typically encounter at Brazil's eastern coast.

The first arrivals were computed in a smoothed velocity model (*i.e.*, macromodel) (Figure 9c). All images that were obtained for this dataset are presented in Figure 10. The RTM image, which was generated using the same smoothed model, exposes a much lower signal-to-noise ratio (Figure 10a) and the noise may be easily mistaken for possible reservoir erroneous seismic facies. Reservoir rugosity would not be an unthinkable misinterpretation to be made from this image assessment. Also, this noise can be responsible for spurious discontinuity of the reflectors.

The Marchenko image that was made with a cross-correlation imaging condition is less noisy – see Figure 10(b). In fact, we observe that the image is clean and that discontinuity is no longer a product of the associated noise seen in the RTM image. When we analyze the results from stabilized deconvolution imaging conditions, the amplitude is much more reliable (Figures 10c and 10d). Evenmore, the continuity of the reflectors seems to honor much better the velocity and density models when we use the initial focusing function to realize the imaging condition (compare Figures 9a and 9b to 10d).

5 Conclusions

We have tested two imaging conditions based on unidimensional stabilized deconvolution. These were applied to the up- and downgoing Green's functions, which were retrieved by the Marchenko method in two synthetic velocity models. The obtained results were compared with the ones from the classic cross-correlation imaging condition, applied both on extrapolated wavefields via Marchenko and via RTM imaging methods. We were able to verify that Marchenko imaging provides cleaner images with less crosstalk from interbed reflections. These ghost reflectors could be interpreted as real events and embarrass interpretation of the images, leading to inaccurate retrieval of rock/reservoir properties and seismic amplitude attributes in general.

When we compare the images obtained from the stabilized deconvolution-based imaging conditions, we can observe clearly the illumination improvement compared to images that are based on cross-correlation. This can be understood since the deconvolution operation provides an amplitude compensation. Moreover, we could notice that the use of the initial focusing function (rather than the full downgoing Green's function) yields an even better resolution and honors the continuity of imaged reflectors. With this approach, ghost artifacts are removed efficiently and crosstalk is avoided because the first event will always be a primary reflection when this imaging condition is used.

However, for even more complex geological situations, better approximations of the transmission response should be used to compute the initial focusing function. The key idea is that, although an optimal image may be achieved using more sophisticated methods such as multidimensional deconvolution, by applying simpler imaging conditions as proposed and depicted here, one might provide accurate images at a considerable lower cost.

6 Acknowledgements

The authors wish to express their gratitude to PETROBRAS, brazilian agencies Fundação de Amparo à Pesquisa do Estado da Bahia (FAPESB), INCT-GP, CNPq, and FINEP for their financial support. The authors would like to thank the three anonymous reviewer, as well as the Associate Editor, for the opportunities of improvement. Mayara would also like to thank Esteban Diaz, Satyan Singh, Myrna Staring, and Leonardo Bernal for helpful information exchange, Alan Souza, Marcela Bastos, and Ricardo Chartuni, for review and support, and Rafaela Reis for essential guidance, discussions, and review.

List of Figures

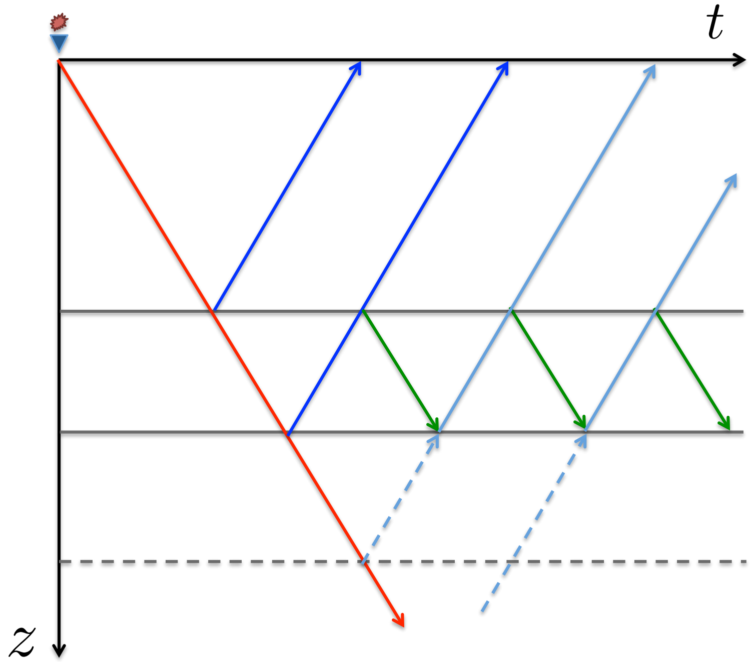

Figure 1: Illustration for 1D multiple scattering from a point source at the surface and events registered at the receivers at the same datum. The real horizontal reflectors are represented by the two continuous black lines; the downgoing direct wavefield by the red arrow; the upgoing primary reflections by the continuous dark blue arrows; the intrabed reflections by the green arrows; the multiple reflections by the light blue arrows. The downward projections of the continuous light blue arrows, depicted by the dashed light blue arrows, describe the origin of ghost reflectors – dark gray dashed horizontal line – created because of the single-scattering assumption incorporated by the conventional imaging methods. (Modified from Behura et al., 2014.)

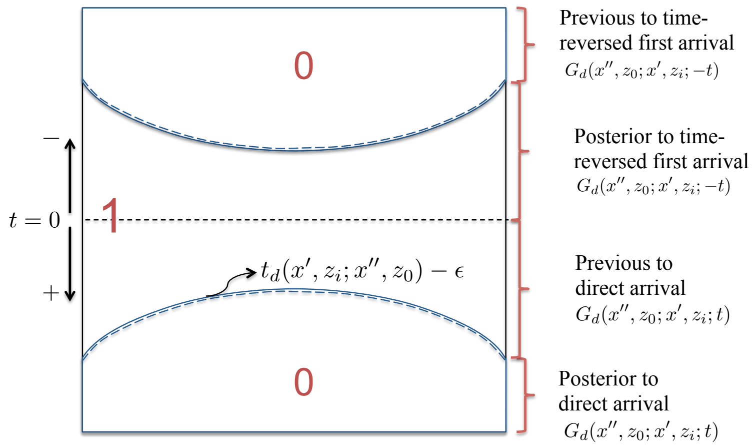

Figure 2: Schematic representation of the window matrix design Θ, which imposes the causality condition to the equations system (5) analysis. Events that occur after or at the same time of the direct arrival (region bellow the inferior continuous blue line, for $t \geq t_d(x', z_i; x'', z_0)$) are eliminated, as well as the events that occur earlier than time-reversed first arrival, imposed by the filter's symmetry.

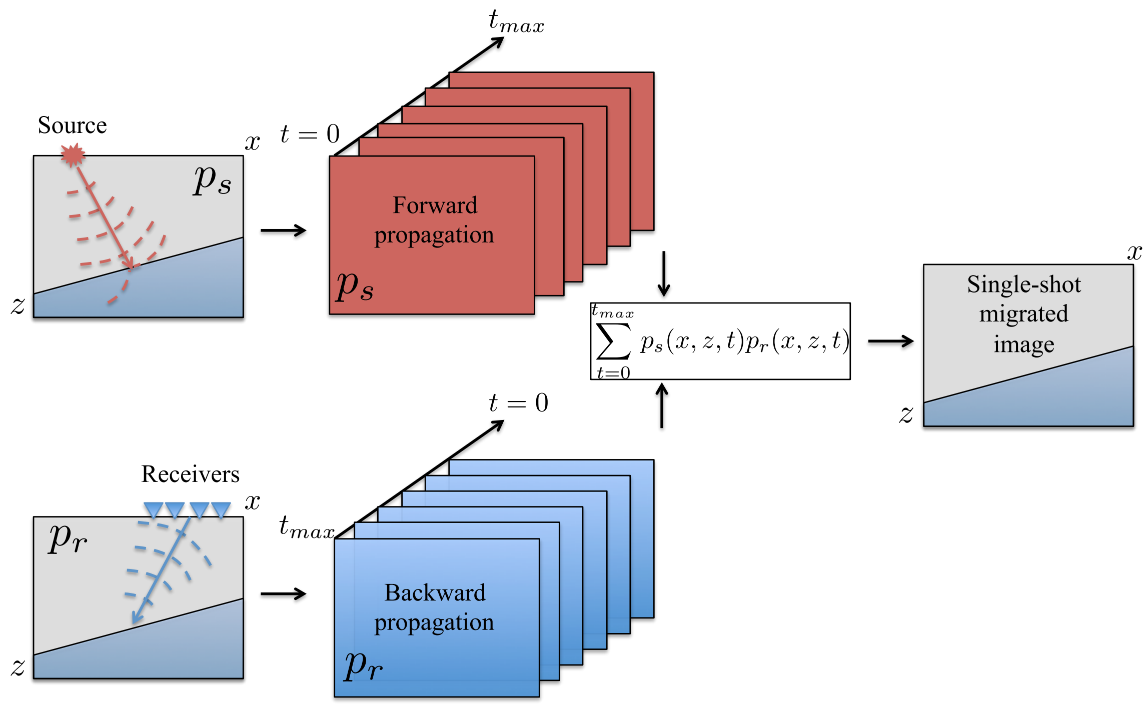

Figure 3: Schematic depict of prestack reverse-time migration of full wavefields flow for a single shot. The RTM algorithm consists of three main steps: forward propagation of the source wavefield; backward propagation of the receiver wavefield; and applying the imaging condition, which is given by the time summation in equation (12).

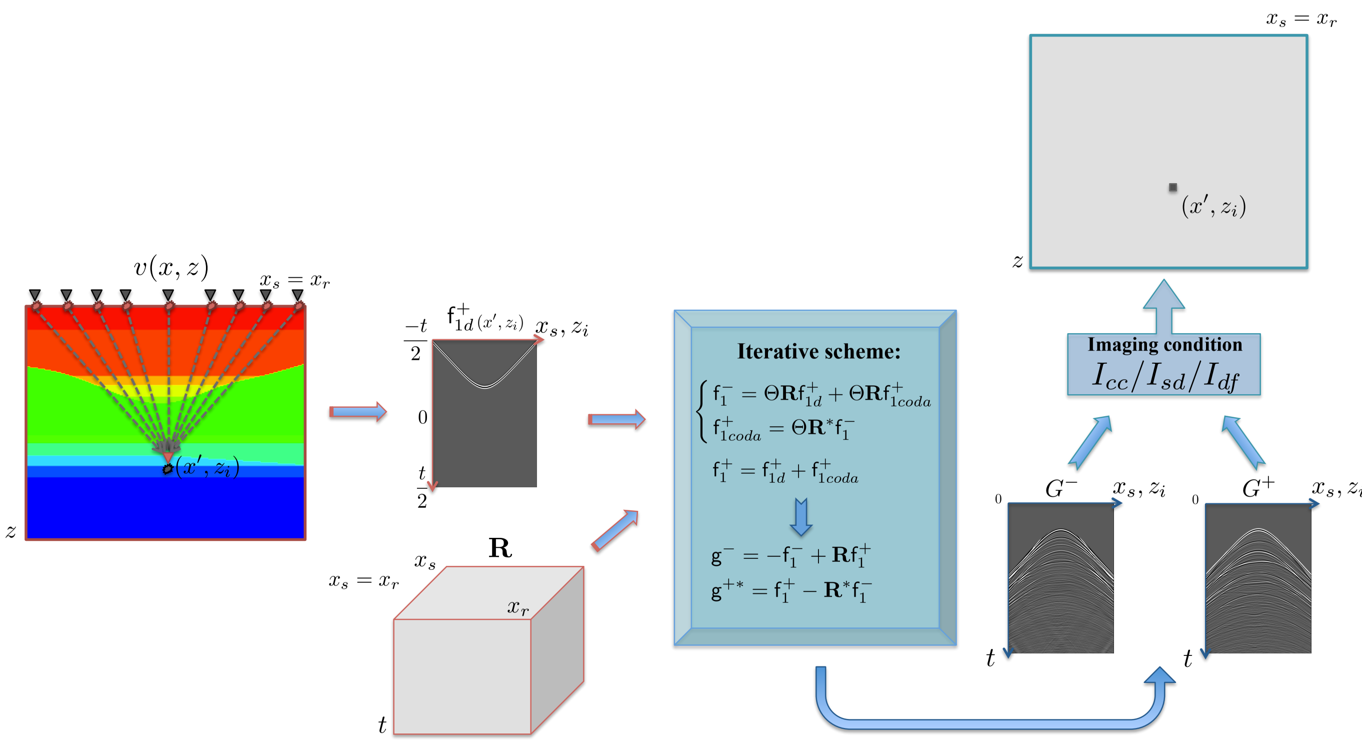

Figure 4: Marchenko imaging scheme workflow, from redatuming to the final image for a single focal point in subsurface. Following the thick arrows orientation, we have the computation of the initial focusing function in a macromodel $v(x,z)$ for the focal point at $(x', z_i) = \mathbf{x_I}$ (leftmost). Together with the observed data (element of the matrix $\mathbf{R}$ - items 1 to 3 of Algorithm 1), f_{1d}^+ is the input for the iterative scheme of the coupled Marchenko equations that solves for the focusing functions. The up- and downgoing Green's function components are retrieved, *i.e.*, the redatumed fields ($\mathsf{g}^- = G^-$ and $\mathsf{g}^+ = G^+$) are obtained. These outputs are combined by applying an imaging condition. Finally, the image for the arbitrary point in the subsurface is constructed.

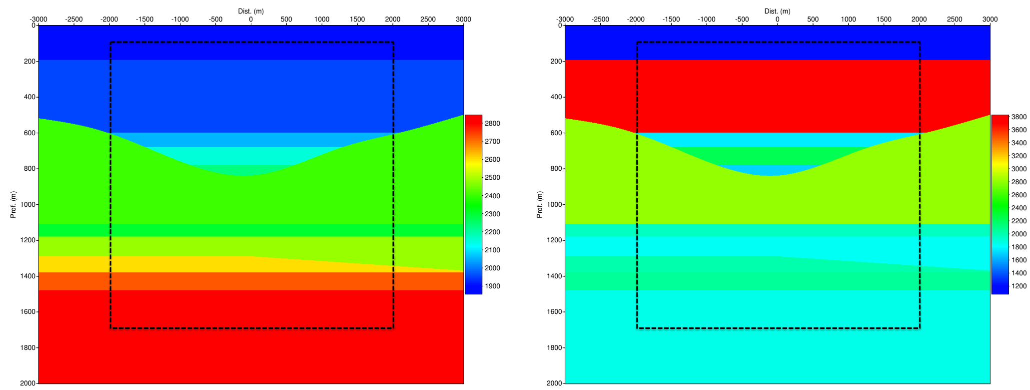

(a) (b)

Figure 5: Syncline velocity (a) and density (b) models, in m/s and kg/m^3, respectively. The region inside the black dashed line is the target area for imaging with Marchenko and comparison with the RTM image.

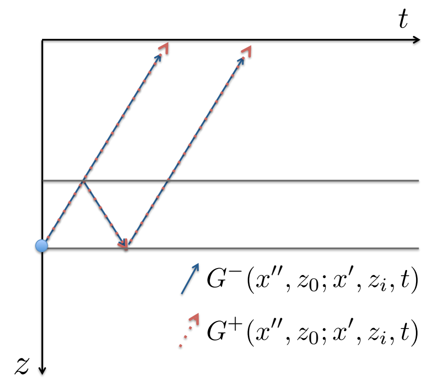

(a)

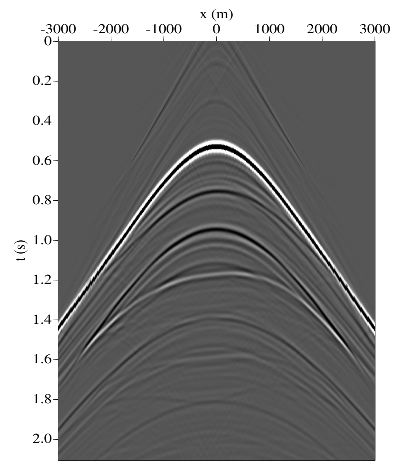

(b)

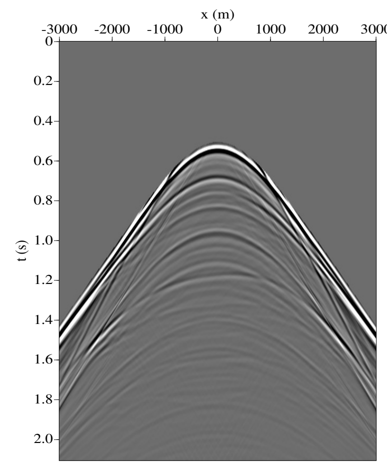

(c)

Figure 6: (a) 1D scheme for the Claerbout image construction principle for a focal point (blue dot) in subsurface in the presence of interbed scattering (modified from Behura et al., 2014). The continuous blue line is the upgoing redatumed wavefield G^-, and the red dashed line represents the downgoing wavefield G^+ (source-receiver reciprocity has been applied for easier visual understanding). The image point is on the reflector and hence imaging operators are time coincident, kinematically in phase. However, their amplitudes commonly differ by the reflection coefficient magnitude (which may be exploited by a deconvolution imaging condition). (b) and (c) show the imaging operators G^+ and G^-, respectively, for depth 1100 m of the syncline model (Figure 5).

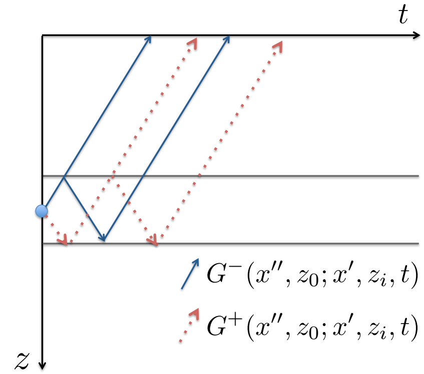

(a)

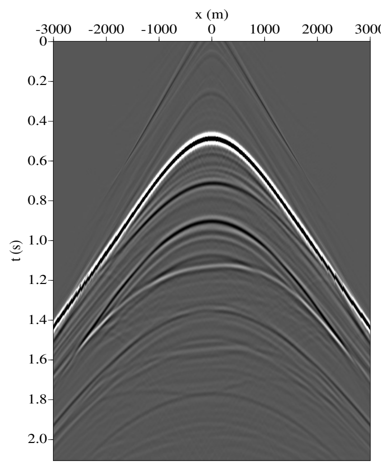

(b)

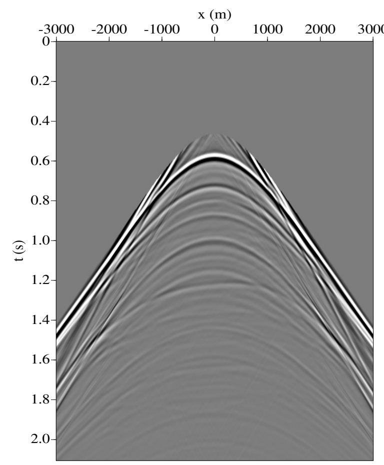

(c)

Figure 7: (a) 1D scheme for the Claerbout image construction principle for a focal point (blue dot) in the subsurface in the presence of interbed scattering (modified from Behura et al., 2014). The continuous blue line is the upgoing redatumed wavefield G^-, and the red dashed line represents the downgoing wavefield G^+ (source-receiver reciprocity has been applied for easier visual understanding). The image point does not coincide with a reflector and hence imaging operators are not in phase, therefore no image is constructed. (b) and (c) show the imaging operators G^+ and G^-, respectively, for depth 1000 m of the syncline model (Figure 5).

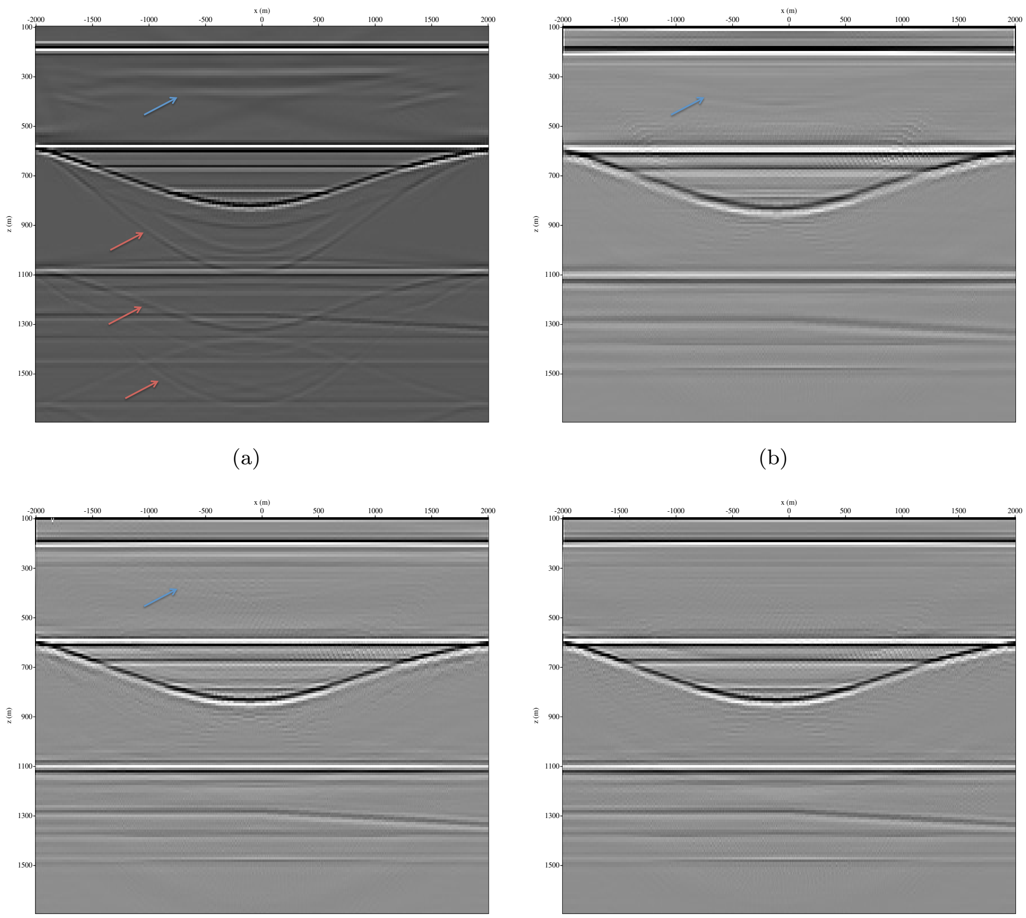

(a) (b) (c) (d)

Figure 8: Comparison of images from distinct imaging conditions applied for the syncline model. (a) RTM image for reference with very apparent internal multiples (pointed out by the red arrows) and poor illumination of the lower portion of the image. (b) shows the classic imaging condition (I_{cc}) applied to Marchenko redatumed fields: a weak ghost artifact is present between 300 m and 500 m (pointed out by the blue arrow). (c) and (d) depict results from the stabilized deconvolution imaging conditions proposed: only using the Green's functions (I_{sd}), and incorporating the time-reversed direct arrival (I_{df}), respectively. Notice the slight improvement of the amplitudes and complete removal of the artifact between 300 m and 500 m, pointed out by the blue arrow, from (c) to (d). Nonetheless, all Marchenko images are cleaner concerning multiply scattered events in comparison to RTM (a Laplacian filter has been applied to all images.)

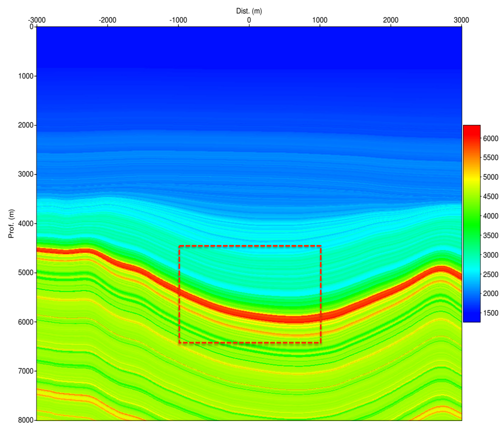

(a)

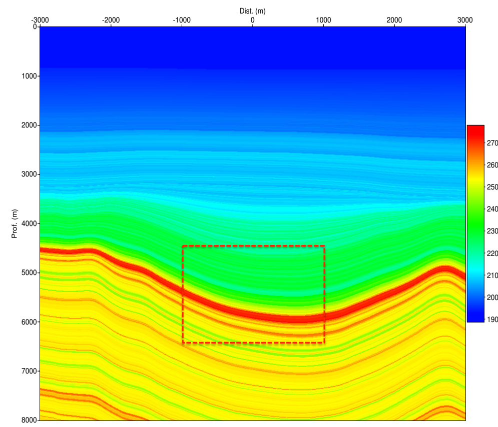

(b)

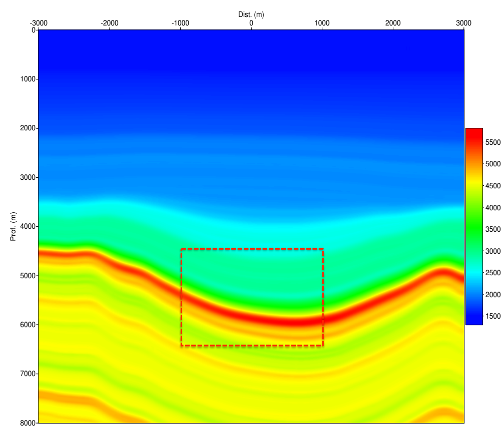

(c)

Figure 9: Thinly layered structure with smooth lateral velocity variation (a) and density (b) of Santos Basin synthetic model. Velocity macromodel in (c). The region inside the red dashed line is the target area for imaging with Marchenko and comparison with the RTM image.

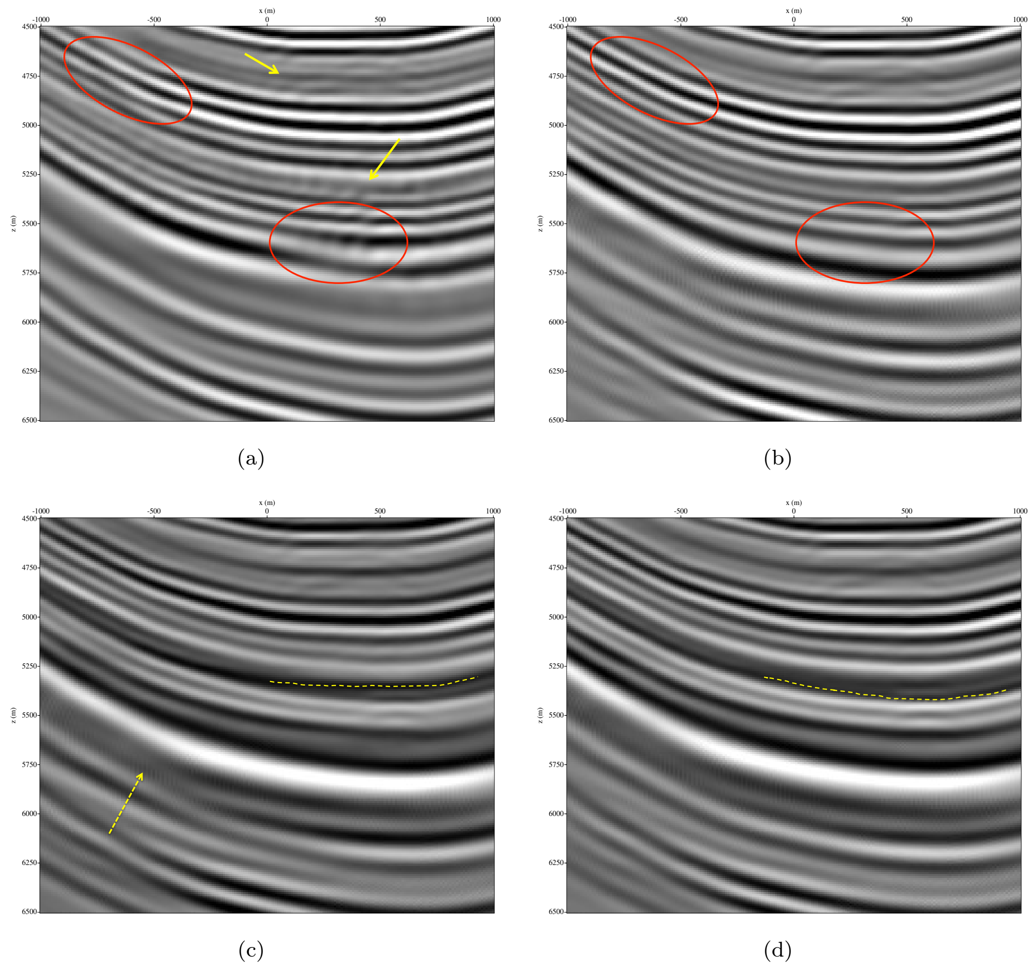

Figure 10: Comparison between images from distinct imaging conditions applied for the Santos Basin synthetic model. (a) RTM image for reference with noticeable noise present and inaccurate amplitudes (red circled areas and some regions are pointed out by yellow arrows) – a Laplacian filter has been applied. (b) shows the correlation-based imaging condition (I_{cc}) applied to Marchenko redatumed fields, resulting in a cleaner image compared to (a) (highlighted by the red circled areas), but the amplitude response is still inaccurate because of the cross-correlation process. (c) and (d) depict the results of resorted stabilized deconvolution image conditions proposed: only using the Green's functions (I_{sd}), and incorporating the time-reversed direct arrival (I_{df}), respectively. Both images expose more accurate amplitudes. Improvement of the reflector continuity is observed from (c) to (d) (see for instance the dashed yellow arrow in (c) and the horizon interpretation by the dashed yellow line). All Marchenko images are cleaner in comparison to the RTM image.

References

Amundsen, L., 2001, Elimination of free-surface-related multiples without need of the source wavelet: Geophysics, **66**, 327–341.

Behura, J., K. Wapenaar, and R. Snieder, 2014, Autofocus imaging: image reconstruction based on inverse scattering theory: Geophysics, **79**, A19–A26.

Berkhout, A. J., 2017, Utilization of multiple scattering: the next big step forward in seismic imaging: Geophysical Prospecting, **65**, 106–145.

Berkhout, A. J. and D. J. Verschuur, 2006, Imaging of multiple reflections: Geophysics, **71**, SI209–SI220.

Broggini, F. and R. Snieder, 2012, Connection of scattering principles: a visual and mathematical tour: Eur. J. Phys., **33**, 593–613.

Broggini, F., R. Snieder, and K. Wapenaar, 2014a, Data-driven Green's function retrieval and application to imaging with multidimensional deconvolution: J. geophys. Res. Solid Earth, **119**, 425–441.

———, 2014b, Data-driven wavefield focusing and imaging with multidimensional deconvolution: numerical examples for reflection data with internal multiples: Geophysics, **79**, WA107–WA115.

Chang, W. and G. A. McMechan, 1986, Reverse-time migration of offset vertical seismic profiling data using the excitation-time imaging condition: Geophysics, **51**, 67–84.

Claerbout, J. F., 1971, Toward a unified theory of reflector mapping: Geophysics, **36**, 467–481.

da Costa Filho, C. A. and A. Curtis, 2016, Attenuating multiple-related imaging artifacts using combined imaging conditions: Geophysics, **81**, S469–S475.

da Costa Filho, C. A., G. A. Meles, and A. Curtis, 2017, Elastic internal multiple analysis and attenuation using marchenko and interferometric methods: Geophysics, **82**, Q1–Q12.

de Hoop, A. T., 1995, Handbook of radiation and scattering of waves: Academic Press.

Dukalski, M. and K. de Vos, 2017, Marchenko inversion in a strong scattering regime including surface-related multiples: Geophysical Journal International, **212**, 760–776.

Faria, E. L. and P. L. Stoffa, 1994, Traveltime computation in transversely isotropic media: Geophysics, **59**, 272–281.

Fleury, C., 2013, Increasing illumination and sensitivity of reverse-time migration with internal multiples: Geophysical Prospecting, **61**, 891–906.

Gardner, G. H. F., L. W. Gardner, and A. R. Gregory, 1974, Formation velocity and - The diagnostic basics for stratigraphic traps: Geophysics, **39**, 770–780.

Guitton, A., 2002, Shot-profile migration of multiple reflections: SEG Technical Program Expanded Abstracts, 1296–1299.

Jia, X., A. Guitton, and R. Snieder, 2018, A practical implementation of subsalt marchenko imaging with a gulf of mexico dataset: Geophysics, **83**, 1–57.

Lomas, A. and A. Curtis, 2018, 3d Marchenko Redatuming Using 2D and 3D Seismic Data: Expanded Abstracts, **80th EAGE Conference and Exhibition**.

Malcolm, A. E., B. Ursin, and V. Maarten, 2009, Seismic imaging and illumination with internal multiples: Geophysical Journal International, **176**, 847–864.

Meles, G. A., K. Wapenaar, and A. Curtis, 2016, Reconstructing the primary reflections in seismic data by marchenko redatuming and convolutional interferometry: Geophysics, **81**, Q15–Q26.

Muijs, R., J. O. Robertsson, and K. Holliger, 2007, Prestack depth migration of primary and surface-related multiple reflections: Part I-Imaging: Geophysics, **72**, S59–S69.

Ong, C., C. Lapilli, J. Perdomo, R. Coates, et al., 2013, Extended imaging and illumination in wave migrations: Presented at the 2013 SEG Annual Meeting.

Ortiz, L. L., 2015, Método *One-step* para modelagem usando os polinômios de Chebyshev e uma condição de imagem para migração com a equação unidirecional da onda: Dissert. de Mestrado, Universidade Federal da Bahia, Salvador, Brasil.

Pestana, R. and P. Stoffa, 2010, Time evolution of the wave equation using rapid expansion method: Geophysics, **75**, T121–T131.

Ravasi, M., 2017, Rayleigh-Marchenko redatuming for target-oriented, true-amplitude imaging: Geophysics, **82**, S439–S452.

Santos, A. W. G., R. C. Pestana, and E. S. Araujo, 2012, Atenuação de artefatos da migração reversa no tempo: Presented at the V Simpósio Brasileiro de Geofísica.

Schleicher, J., J. C. Costa, and A. Novais, 2008, A comparison of imaging conditions for wave-equation shot-profile migration: Geophysics, **73**, S219–S227.

Singh, S. and R. Snieder, 2017, Strategies for imaging with Marchenko-retrieved Greens functions: Geophysics, **82**, 1–68.

Singh, S., R. Snieder, J. van der Neut, E. Slob, and K. Wapenaar, 2017, Accounting for free-surface multiples marchenko imaging: Geophysics, **82**, R19–R30.

Slob, E., K. Wapenaar, F. Broggini, and R. Snieder, 2014, Seismic reflector imaging using internal multiples with Marchenko-type equations: Geophysics, **79**, S63–S76.

Slob, E. C. and K. Wapenaar, 2017, Theory for Marchenko Imaging of Marine Seismic Data with Free Surface Multiple Elimination: Expanded Abstracts, **79th EAGE Conference and Exhibition**.

Staring, M., N. Grobbe, J. van der Neut, and K. Wapenaar, 2017, Sparse Iversion for Solving the Coupled Marchenko Equations Including Free-surface Multiples: Expanded Abstracts, **79th EAGE Conference and Exhibition**.

Thorbecke, J., E. Slob, J. Brackenhoff, J. van der Neut, and K. Wapenaar, 2017, Implementation of the Marchenko method: Geophysics.

Thorbecke, J., J. van der Neut, and K. Wapenaar, 2013, Green's function retrieval with Marchenko equations: a sensitivity analysis: SEG Technical Program Expanded Abstracts, **83rd Annual International Meeting**.

Thorbecke, J. W. and D. Draganov, 2011, Finite-difference modeling experiments for seismic interferometry: Geophysics, **76**, H1–H18.

Valenciano, A. and B. Biondi, 2003, 2d deconvolution imaging condition for shot profile migration: 73rd Ann. Internat. Mtg., Soc. of Expl. Geophys., Expanded Abstracts, 1059–1062.

van der Neut, J., J. Thorbecke, K. Mehta, E. Slob, and K. Wapenaar, 2011, Controlled-source interferometric redatuming by crosscorrelation and multidimensional deconvolution in elastic media: Geophysics, **76**, SA63–SA76.

van der Neut, J., I. Vasconcelos, and K. Wapenaar, 2015, On Green's function retrieval by iterative substitution of the coupled Marchenko equations: Geophys. J. Int., **203**, 792–813.

Vasconcelos, I., D. J. van Manen, M. Ravasi, K. Wapenaar, and J. van der Neut, 2014, Marchenko redatuming: advantages and limitations in complex media: SEG Technical Program Expanded Abstracts, **Workshop W-11, 84th Annual Meeting**.

Vasconcelos, I., K. Wapenaar, J. van der Neut, C. Thomson, and M. Ravasi, 2015, Using inverse transmission matrices for marchenko redatuming in highly complex media: SEG Technical Program Expanded Abstracts, **85th Annual International Meeting**, 5081–5086.

Verschuur, D. J., A. J. Berkhout, and C. P. A. Wapenaar, 1992, Adaptative surface-related multiple elimination: Geophysics, **57**, 1166–1177.

Wang, Y., H. Sun, and G. T. Schuster, 1999, Migration imaging condition for primary reflections: Presented at the 1999 SEG Annual Meeting.

Wapenaar, C. P. A. and J. L. T. Grimberg, 1996, Reciprocity theorems for one-way wave fields: Geophys. J. Int., **127**, 169–177.

Wapenaar, K., D. Draganov, and J. O. A. Robertsson, 2008, Redatuming, chapter 5, 331–448. Geophysics Reprint Series.

Wapenaar, K., J. Fokkema, M. Dillen, and P. Scherpenhuijsen, 2000, One-way acoustic reciprocity and its applications in multiple elimination and time-lapse seismics: Presented at the SEG Annual Meeting.

Wapenaar, K., J. Thorbecke, J. van der Neut, F. Broggini, E. Slob, and R. Snieder, 2014a, Green's function retrieval from reflection data, in absence of a receiver at the virtual source position: J. acoust. Soc. Am., **135**, 2847–2861.

———, 2014b, Marchenko imaging: Geophysics, **79**, WA39–WA57.

Weglein, A. B., F. V. Araújo, P. M. Carvalho, R. H. Stolt, K. H. Matson, R. T. Coates, D. Corrigan, D. J. Foster, S. A. Shaw, and H. Zhang, 2003, Inverse scattering series and seismic exploration: Inverse Probl., **19**, R27.

Zhang, Y., J. Sun, and S. Gray, 2007, Reverse-time migration: Amplitude and implementation issues, *in* SEG Technical Program Expanded Abstracts, 2145–2149, Society of Exploration Geophysicists.

Zhou, M., H. Sun, and G. T. Schuster, 2003, The application of primary-only imaging condition to smaart data: Presented at the 2003 SEG Annual Meeting.